NJC

ROYAL SOCIETY OF CHEMISTRY

PAPER

View Article Online
View Journal | View Issue

Cite this: *New J. Chem.*, 2024, **48**, 9909

Interface properties of hydroxyapatite in ternary composites cathodes for electromethanogenesis†

Michele Bigica, [a] Giorgia Ghiara, [b] Pierangela Cristiani, *[c] Sebastiano Campisi *[a] and Antonella Gervasini [a]

The bioelectrochemical conversion of CO_2 to CH_4 (electromethanogenesis), using renewable energy, is a promising power-to-gas technology. However, maximizing its potential requires the development of cost-effective materials for biocathodes. A recent research achieved significant progress by employing a ternary composite material comprising porous carbon (biochar) modified with 20 wt% copper and 10 wt% hydroxyapatite (HAP). Notably, the addition of HAP led to a remarkable increase in methane production compared to undoped biochar and Cu-doped biochar, reaching a maximum of 0.87 mol m^{-2} d^{-1} with a coulombic efficiency of 64%. Based on these results, this study aims to elucidate the pivotal role of hydroxyapatite as a crucial modifier in biochar-based cathode materials. Employing a range of characterization techniques such as N_2 adsorption/desorption isotherms, solid–liquid phase titrations with probe molecules, electron microscopy, and infrared spectroscopy, the research delved into the unique contributions of hydroxyapatite surface features to the electromethanogenesis process on the composite cathode. The results underscored the beneficial effects of HAP in enhancing reagent adsorption, providing a hydrophilic interface beneficial to microbial adhesion, and stabilizing the interface pH. This comprehensive investigation sheds light on the factors underlying the enhanced performance of bioelectrochemical systems facilitated by HAP-modified cathode materials.

Received 5th March 2024,
Accepted 8th May 2024

DOI: 10.1039/d4nj01053a

rsc.li/njc

Introduction

Carbon capture and utilization (CCU) technologies,[1] developed to mitigate CO_2 emissions, encompass chemical, biological, photocatalytic, and electrochemical processes, each offering unique pathways for converting captured CO_2 into valuable products, such as fuels, chemicals, and building materials. CCU technologies can promisingly match with the power-to-gas (P2G) approach, which stands out with the primary target of providing scalable and flexible energy storage solutions that complement intermittent renewable unprogrammable energy sources.[2] In the context of BEP2G approach, the electromethanogenesis process represents a suitable bioelectrochemical technology for large-scale recycling of carbon dioxide (CO_2) emissions using renewable energy to form methane (CH_4). This strategy combines in a single step the biological methanation process with the electro-synthetical approach.[3–8] In conventional biogas plants, methanogenic microorganisms are used to produce biomethane from a limited number of organic substrates (*e.g.*, acetate, formate, and methanol) with the process named dark fermentation. Several methanogens (of the *Archaea* domain) reduce CO_2 or bicarbonate to methane. However, the limited availability of hydrogen from the dark fermentation process limits these hydrogenotrophic microorganisms.[9] On the other hand, pure electrochemical methods for direct methane production from CO_2 involve the use of precious metals and lack of specificity, producing large amounts of undesired long-chain alkanes.[10] The electromethanogenesis process overcomes these limitations combining electrolyzer and bioreactor in a single step process, where hydrogenothropic microorganisms of the *Archea* domain grew over a cathode of the electrochemical system acting as microbial electrocatalysts. Recent studies have tried to elucidate the complex involved mechanisms, which include (i) the most energetically favored direct electron transfer (DET) from cathode to methanogens (eqn (1)), and (ii) the mediated electron transfer (MET) from electrochemically produced hydrogen (eqn (2)) to hydrogenothropic microbes (eqn (3)).[11,12]

Direct electron transfer (DET)

$$CO_2 + 8H^+ + 8e^- \rightarrow CH_4 + 2H_2O \quad E^\circ = -0.24\ \text{V (}vs.\ \text{SHE, } T = 25\ ^\circ\text{C, pH} = 7\text{)} \qquad (1)$$

[a] *Università degli Studi di Milano, Dipartimento di Chimica, 20133 Milano, Italy. E-mail: sebastiano.campisi@unimi.it*
[b] *Università degli Studi di Milano, Dipartimento di Scienze e Politiche Ambientali, 20133 Milano, Italy*
[c] *Ricerca sul Sistema Energetico - RSE S.p.A, 20134 Milano, Italy. E-mail: pierangela.cristiani@rse-web.it*

† Electronic supplementary information (ESI) available. See DOI: https://doi.org/10.1039/d4nj01053a

Mediated electron transfer (MET)

$$2H^+ + 2e^- \rightarrow H_2 \quad E^\circ = -0.41V \text{ (vs. SHE, } T = 25\ ^\circ C, \text{ pH} = 7) \tag{2}$$

$$CO_2 + 4H_2 \rightarrow CH_4 + 2H_2O \tag{3}$$

Due to kinetic limitations and parallel electrode reactions, cathode potential values more negative than the theoretical thermodynamic one must be applied to achieve measurable methane production rates but avoiding an excessive unconverted hydrogen. Strategies to reduce the overpotential would reduce energy requirements allowing to minimize operating costs and optimizing methane yield.

Within recent years, several bioelectrochemical systems have been developed on a laboratory-scale, focusing on the study of the effects of microbial species and dynamics, reactor design and configuration, electron transfer mechanism, composition of feeding gases, and applied cathode potential.[13] The cathode material as well plays a crucial role in facilitating electron transfer and methane production in electromethanogenesis systems.[14] However, the design of high-performing cathode materials still remains a great challenge. The ideal cathode material should offer a large accessible surface area, biocompatibility, cost-efficiency, efficient electron transfer with microorganisms, electrical conductivity, pH buffering ability, maximized mass transfer of substrates/products, improved cell adherence, and corrosion resistance.

Up to now, a wide range of materials have been explored for biocathode construction. Carbon-based electrodes, including graphite, carbon cloth, and carbon felt, have demonstrated robust performance in methane production, with reported efficiencies ranging from 0.4 to 3 mol m^{-2} d^{-1}.[15–21] Conductive polymers (*e.g.*, polyaniline, polypyrrole, acrylonitrile-butadiene-styrene polymers) have shown promising results, enhancing CO_2 conversion, although in these cases acetate was preferentially formed over methane.[22,23] Carrillo-Pena *et al.* demonstrated that the modification of carbon electrodes by reduced graphene oxide promoted biofilm formation and methane production (a methane richness higher than 95% when CO_2 was fed at a rate between 15 and 30 g m^{-2} d^{-1}) compared to unmodified electrodes.[24]

Non-precious metals (Cu, Fe, Ni, Bi, and Sn) have been considered as biocathodes for methane production. Wang *et al.*[25] compared stainless steel mesh, nickel mesh, and copper mesh and obtained the highest methane production (59.2 mL CH_4/gVSS) over the Ni cathode, which corresponded to the most abundant presence of hydrogenotrophic methanogens.

Metals have been studied also in the form of bimetallic alloys[26] or combination with non-metal elements like O, C, S, P, and N in the form of oxides, carbides, sulfides, phosphides, and nitrides.[27,28] Siegert *et al.*[28] compared methane production among metal-based materials (platinum, stainless steel, nickel, ferrihydrite, magnetite, iron sulfide, molybdenum disulfide) and carbon-based materials (carbon brush, carbon black, and plain graphite), finding that the latter produced a higher amount of methane compared to the former.

Drawing from insights in photocatalysis,[29–33] researchers have recently explored the synergistic benefits of composite materials in the field of biocathode applications for electromethanogenesis systems. Kracke *et al.*[34] found that transition metal-based cathodes, such as CoP, MoS_2, and NiMo, assured notable rates, selectivity, and stability in methane (CH_4) and acetate production. Similarly, Gomez *et al.*[35] observed improved CH_4 production rates (reaching 0.83 L L_c^{-1} d^{-1}) by dissolving Ni and Fe salts into the cathodic compartment. This enhancement was attributed to the *in situ* deposition of Ni and Fe on the carbon felt cathode, which enhanced cathode conductivity and promoted electron transfer mechanisms. Qiu *et al.*[36] demonstrated that employing Sn-modified carbon felt improves acetate yield by catalyzing formate production, serving as an electron donor for CO_2 reduction. Thi Vu *et al.*[37,38] have successfully exploited the synergistic effects deriving from composite materials: in particular, a cost-effective magnetite/zeolite nanocomposite demonstrated to boost methane production rate (0.238 L L^{-1} d^{-1}).[38]

Based on our previous experience with conductive carbon-based HAP composites,[39,40] we recently proposed hydroxyapatite ($Ca_{10}(PO_4)_6(OH)_2$, HAP)[41,42] as a key modifier capable of altering the product distribution of Cu-decorated N-doped graphene nanosheets.[43] This modification directs the electrocatalytic reduction of CO_2 towards formate production. Based on these results, we applied the same principles to electromethanogenesis, resulting in the development of an environmentally friendly ternary composite material.

A highly conductive and electroactive biogenic charcoal (biochar),[44] known for its biocompatibility, mechanical resistance, and performance in microbial electrocatalysis,[45] was chosen as the support for copper nanoparticles (Cu NPs). Cu NPs serve as the active phase promoting the reduction of CO_2 to a variety of higher order products, such as CH_4, C_2, or C_3. HAP was then incorporated as a sustainable modifier. Remarkably, biochar loaded with 20% Cu and 10% hydroxyapatite (10HAP-20Cu/C) demonstrated superior performance in electromethanogenesis systems compared to undoped biochar and Cu-doped biochar, resulting in higher biomethane productivity (0.87 mol m^{-2} d^{-1}), and faster kinetics.[46]

Although hydroxyapatite is experiencing a growing success as catalytic support in catalysis[47–49] and photocatalysis,[50,51] thanks to its highly functionalized surface, its role in biocatalysis needs additional research. Hence, this work aimed to investigate the properties of ternary composites combined with HAP, with particular focus on interface properties, as the focal point for microbial adhesion, electron transfer processes, electrode resistance, and reaction kinetics.

Scanning electron microscopy was used to directly study the relation between microorganism distribution and hydroxyapatite nanoparticle location. N_2 adsorption/desorption isotherms were collected to measure the surface area and porosity. Surface acid and basic sites of HAP samples were quantified by online titration in solid–liquid phase with solutions of 2-phenylethylamine (PEA) and phenylacetic acid (PAA), selected as basic and acidic probe molecules, respectively, in cyclohexane as the solvent. The acid–base character of HAP surface was then related to the

adsorption capacity towards bicarbonate anions, which are assumed to be the predominant form of CO_2 in water.

Thorough knowledge of the function of hydroxyapatite in the electromethanogenesis process over ternary composites is not only intriguing from a theoretical standpoint but is also required for the design of effective cathode composite materials for practical applications.

Experimental

Composite preparation

The detailed procedures for the preparation of single components and ternary composite have been reported in previous works.[46,52]

In brief, biochar was produced by pyrolysis of maize stalk canes at 900 °C.

Stoichiometric hydroxyapatite was synthesized by conventional co-precipitation procedure from aqueous solutions of 0.167 M $Ca(NO_3)_2{\cdot}4H_2O$ (>99%, Carlo Erba) and 0.1 M $(NH_4)_2HPO_4$ (>98%, Sigma-Aldrich) at 25 °C and pH > 10 (regulated by 30% NH_4OH addition).

The multicomposite material (biochar doped by 20 wt% Cu NPs and 10 wt% HAP) was produced by combining the obtained biochar, hydroxyapatite and commercial copper nanoparticles (Sigma Aldrich, CAS 7440508, d = 25 nm) in a multi-step protocol. Firstly, biochar powder (*ca.* 80 mg) was dispersed in isopropyl alcohol (IPA, *ca.* 0.04 L) and the pH of the suspension was adjusted to 10 by addition of KOH aqueous solution (0.1 M). Similarly, commercial Cu NPs (*ca.* 20 mg) were dispersed in IPA (0.04 L), adjusting the pH as indicated for the biochar suspension. Both mixtures were sonicated and then, the Cu NP suspension was added one shot to the biochar suspension. The resulting mix was kept under stirring at 25 °C for 48 h and then filtered under vacuum on a 0.45 μm Nylon membrane, thoroughly washed with MilliQ water, and dried at 110 °C. Cu/C composite (100 mg) was suspended in MilliQ water (*ca.* 0.09 L). The pH of the suspension was fixed to 7 by adding KOH (0.1 M). Similarly, HAP (*ca.* 11 mg) was dispersed in MilliQ water (*ca.* 0.02 L), adjusting the pH of the suspension to 7 by adding a KOH (0.1 M) solution. Both suspensions were sonicated for 45 minutes. Then, the HAP suspension was added to the Cu/C suspension; the mixture was stirred for 72 h at 25 °C. The powder was vacuum filtered on a 0.45 μm Nylon membrane, washed with MilliQ water and dried at 110 °C for 3 h.

X-Ray powder diffraction (XRPD) pattern of the composite was collected using a Philips PW3020/PW1830 powder diffractometer operating with an X-ray source at 40 kV and 40 mA in the range between 5°–60°(2θ), step of 0.02° 2θ and scan rate of 0.6° min^{-1}.

Material surface characterization

X-Ray photoelectron spectroscopy (XPS) was employed to study the surface composition of the samples. Measurements were carried out using the M-PROBE Surface Spectrometer, with an Al (Ka) source and a spot size from 0.15 mm to 1 mm in diameter. The applied voltage was 10 V at a vacuum of 10^{-7}–10^{-8} Torr. The survey scans were carried out in the binding energy interval from 0 to 1100 eV, using a spot size of 800 microns. The energy resolution was 4 eV and the scan rate was 1 eV per step. The software used for data analysis was ESCA Hawk Software.

N_2 adsorption–desorption isotherms were collected at liquid nitrogen temperature, by means of a Sorptomatic 1990 version instrument from Thermo Scientific (Carlo Erba). Surface area (SA) and pore size distribution (PSD) of analyzed samples have been determined according to 2-parameter BET (Brunauer–Emmett–Teller) equation (adsorption branch, $0.05 < p/p^0 < 0.4$) and B. J. H. (Barrett–Joyner–Halenda) model (desorption branch, $0.3 < p/p^0 < 0.95$), respectively. Prior to the analysis, the samples were pressed, crushed and sieved to obtain particles in the range of 80–200 mesh. Then, the samples (whose mass was selected according to the expected surface area) were outgassed at 300 °C for 16 h (biochar and composite) or at 150 °C for 16 h (bare HAP) under vacuum to remove water and other volatile organic compounds adsorbed on the surface.

Surface acid and basic sites of HAP sample were measured in liquid by titration with solutions of 2-phenylethylamine (PEA) and phenyl acetic acid (PAA), respectively. Titrations were carried out in cyclohexane for the intrinsic acidity and basicity (I.A. and I.B.) HAP sample (*ca.* 0.08 g, crushed and sieved as 80–200 mesh particles) was placed in a sample holder (stainless steel tube, 2 mm diameter and 12 cm of length) between two sand pillows. HAP sample was then activated by thermal treatment (150 °C in 8 mL min^{-1} air flux for 16 h) and successively filled with cyclohexane. The sample holder was then mounted on a recirculation chromatographic line (HPLC), equipped with Waters 515 pump and monochromatic UV detector (Waters, model 2487, working at fixed λ = 254 nm). During the analyses, the sample was maintained at constant temperature (30.0 ± 0.1 °C). The collected isotherms were interpreted following the Langmuir model (eqn (4)):

$$\frac{\text{probe}_{\text{ads}}}{\text{probe}_{\text{ads,max}}\dfrac{b_{\text{ads}}[\text{probe}]_{\text{eq}}}{\left(1+b_{\text{ads}}[\text{probe}]_{\text{eq}}\right)}} \quad (4)$$

where, $\text{probe}_{\text{ads}}$ and $\text{probe}_{\text{ads,max}}$ indicate the amount of probe (PEA or PAA) adsorbed and the maximum amount of probe adsorbed by the surface, $[\text{probe}]_{\text{eq}}$ indicates the probe concentration in solution at equilibrium, and b_{ads} is the Langmuir constant. From the conventional linearized equation, reporting $[\text{probe}]_{\text{eq}}/[\text{probe}]_{\text{ads}}$ *vs.* $[\text{probe}]_{\text{eq}}$, the values of $\text{probe}_{\text{ads,max}}$ (mmol g^{-1}) could be obtained. Assuming a 1 : 1 stoichiometry for the probe adsorption on the acid site, the value of $\text{probe}_{\text{ads,max}}$ of the I run isotherm gives the total number of acid sites, while the value of $\text{probe}_{\text{ads,max}}$ obtained from the II run isotherm corresponded to the number of weak acidic sites. The number of strong acid sites was obtained by the difference between the number of total and weak sites.

All the details on the operative and interpretative procedures can be found elsewhere.[53,54]

Thermo-desorption analyses were carried out using ammonia (NH_3-TPD) or sulphur dioxide (SO_2-TPD), as basic and acid probe, respectively, by operating in a homemade adsorption/desorption line. The line was equipped with a set of mass flow controllers (Bronkhorst, Hi-Tec and Brooks Instruments), a tubular vertical electric oven (Eurotherm controller-programmer type 818), a quartz tubular sample-holder with a porous septum (5 mm i.d.) for positioning the sample (*ca.* 0.1 g, 80–200 mesh particle size) and an online FT-IR spectrophotometer (Bio-Rad, DTGS detector). Adsorption and desorption were followed by continuous monitoring of selected IR lines (926 cm^{-1} for NH_3 and 1360 cm^{-1} for SO_2) as a function of temperature. Surface saturation was performed at 80 °C on thermally activated samples (120 °C for 30 min) under 50 ml min^{-1} total flow. After reaching surface saturation, an isothermal step at 150 °C was performed to remove the excess of adsorbed ammonia (physisorbed) from the sample surface until a stable signal was obtained. Then, the temperature was raised by 20 °C min^{-1} up to 800 °C.

Scanning electron microscopy analysis

The distribution of microorganisms onto multicomposite was investigated by scanning electron microscopy analysis (SEM) JSM-IT 500 (JEOL, 2019) coupled with Energy dispersive X-Ray measurements (EDS) at Department of Earth Sciences of the University of Milan. The analyses were performed at different magnifications and with an acceleration voltage of 20 KeV using a secondary electrons detector (SED, JEOL).

Carbonate/bicarbonate uptake tests

The sorption ability of pristine HAP, biochar and composite towards bicarbonate anions has been evaluated by means of stirred batch adsorption tests. A weighed amount of solid sample (*ca.* 500 mg) was placed in test tube, equipped with magnetic stirrers and contacted with 40 mL of 5.5 mM $NaHCO_3$ solutions (>99%, purchased from Carlo Erba). All solutions were prepared using MilliQ water (15.2 MΩ, Millipore).

Adsorption tests have been carried out at T = 30 °C and with a contact time of 8 hours.

The residual concentration of bicarbonate was determined by potentiometric titration. At the end of each test the solid material was separated by single filtration and two aliquots (20.0 mL) of each obtained solution were titrated with aqueous HCl solution (5 mM). The absorbed amount of bicarbonate (q_{HCO3}, in mmol g^{-1}) was calculated by:

$$q_{HCO_3} = \left[\frac{\left(C^0_{HCO_3} \cdot V^0_{HCO_3}\right) - (2C_{HCl} \cdot V_{HCl})}{m}\right] \quad (5)$$

where $C^0_{HCO_3}$ is the concentration of $NaHCO_3$ solution (5.5 mmol L^{-1}), C_{HCl} is the concentration of HCl solution (5 mmol L^{-1}), $V^0_{HCO_3}$ is the volume of $NaHCO_3$ solution (L) in put contact with the solid sample, V_{HCl} is the volume of HCl spent in the titration of non-adsorbed bicarbonate's excess (L) and m is the mass of solid sample (g).

Blank titrations were performed on 5.5 mM $NaHCO_3$ solutions.

Transmission Fourier transform infrared (FT-IR) spectra on HAP samples (pelletized in anhydrous KBr), before and after adsorption experiments, were collected at RT in the wavenumber range from 500 cm^{-1} to 4000 cm^{-1}, by means of a PerkinElmer Spectrum Two Fourier transform infrared spectrometer.

Electrochemically active surface area (ECSA) determination

Electrochemically active surface area (ECSA) measurements were performed on the suitably prepared composite material (geometric surface area of 1 cm^2), operating in the same conditions used for the cathode of an electromethanogenesis system (polarized at −1.2 V *vs.* Ag/AgCl) and without polarization. The catholyte was inoculated with hydrogenotrophic microorganisms from an operating bioreactor, consisting mainly of Methanobacterium order.[46] Measurements were performed during two weeks of test (at 1, 7 and 14 days). Voltammetric curves (CV) of the polarized multicomposites were performed at open circuit potential (OCP) after a suitable equilibration time. The system consisted of a three-electrode cell with the sample as the working electrode (WE), a saturated Ag/AgCl as the reference electrode (RE) and a Ti-mesh as the counter electrode (CE). The determination of the ECSA was carried out in the vicinity of the open circuit potential (±50 mV *vs.* OCP) and at different scan rates (from 10 to 100 mV s^{-1}) to determine the variation of the double layer capacitance (C_{dl}), with time and indirectly the performance of the substrate. Measurements were replicated twice to have a statistical meaning of the data.

Results and discussion

An innovative and cost-effective composite material (10HAP-20Cu/C), consisting of porous carbon (biochar, C) doped with 20 wt% copper (Cu) and 10 wt% hydroxyapatite was prepared according to a multi-step protocol, already presented in the literature.[46,52]

X-ray powder diffraction (XRPD) analysis (Fig. 1A) and X-ray photoelectron spectroscopy (XPS) measurements (Fig. 1B–D) confirmed the successful immobilization of both Cu and HAP onto the biochar surface.

The XRPD pattern (Fig. 1A) revealed a dominant broad peak at 2θ of 20°–30°, attributable to the (0 0 2) plane of aromatic layers, indicating the presence of small graphitic domains within the biochar structure. Copper existed predominantly as copper nanoparticles in metallic form (JCPDS 01-070-3038), with characteristic reflections observed at 2θ of 43.2° (1 1 1) and 50.0° (2 0 0). Additionally, partial oxidation of Cu was evident from the peak at 36.5°, corresponding to the (1 1 1) plane of cubic Cu_2O (JCPDS 00-065-3288). Crystalline hydroxyapatite reflections (26° and 32°), consistent with JCPDS 00-064-0738, were also detected, despite their low intensity due to the relatively low content (10 wt%, close to the detection limit).

XPS analysis provided valuable insights into surface species (Fig. 1B), with signals corresponding to Ca 1s (2.3 atom%), P 2p

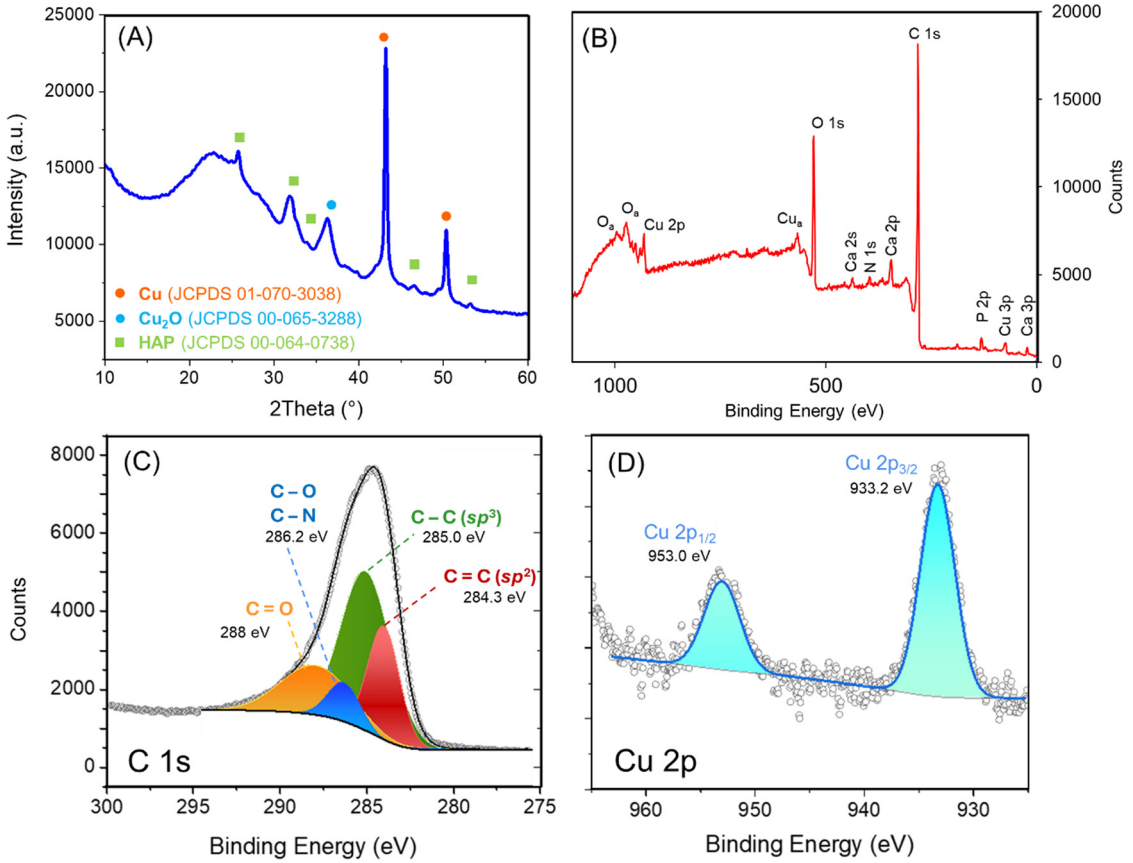

Fig. 1 Bulk and surface characterization of 10HAP-20Cu/C composite. (A) XRPD pattern; (B) XPS survey scan; high-resolution XP spectra for (C) C 1s and (D) Cu 2p.

(2.2 atom%), characteristic of HAP, and Cu 2p (1.2 atom%) observed in the survey XPS scan, confirming the enrichment of HAP and Cu on the biochar surface. In addition, the survey spectrum presented peaks corresponding to C 1s (75 atom%) and O 1s (17 atom%), with impurities of N (2.4 atom%). Further deconvolution of the high-resolution C 1s XP spectrum (Fig. 1C) revealed bands attributed to π-hybridized carbon C═C (at ∼284.3 eV), sp^3-hybridized carbon C–C/C–H (at ∼285 eV), along with minor contributions from oxygen functional groups (C–O, C–O–C, C═O, and OC═O, 286–288 eV).[55] The high-resolution Cu 2p spectrum (Fig. 1D) exhibited peaks at binding energies of 932.3 eV and 953 eV, corresponding to Cu $2p_{3/2}$ and Cu $2p_{1/2}$, respectively. The peak positions, along with the absence of satellite peaks, indicated that surface copper species predominantly existed in a single oxidation state of Cu(I),[56] consistent with the XRPD findings and confirming surface passivation of Cu nanoparticles with the formation of a thin layer of Cu_2O.

The bioelectrochemical reduction of CO_2 takes place in a complex system, governed by multiple interactions, which involve microorganisms, electrode materials and the solution components. Hydroxyapatite, when inserted in a multi-composite electrode, is expected to create a biointerface able to promote the adhesion of microorganisms and their growth as well as to mediate the interactions with reagent and products. Consequently, to unravel the active role of hydroxyapatite in the studied ternary composites, different aspects need to be discriminated and studied.

Morphological properties (specific surface area and porosity) of HAP, biochar and composite were determined by N_2 adsorption/desorption at −196 °C. The obtained adsorption/desorption isotherms are reported in Fig. 2(a)–(c). According to the IUPAC classification of physisorption isotherms,[57] the adsorption isotherm of HAP was of Type IV, with a well-developed mesoporosity, evidenced by the presence of hysteresis zone. The specific surface area of HAP was 96 $m^2\ g^{-1}$ as computed by 2-parameters BET model. The pore distribution resulted to be in the range of mesoporous materials (2–50 nm), centered in the range 4–12 nm. The N_2 adsorption/desorption isotherm of biochar displays the usual type-II profile, indicating that the carbon includes exclusively macropores. The surface area of biochar (SSA 9 $m^2\ g^{-1}$) resulted to be 10-fold lower than that of HAP.

It is noteworthy that the deposition of 10 wt% hydroxyapatite and 20 wt% of Cu NPs (SSA of 27 $m^2\ g^{-1}$) onto biochar resulted in a remarkable increase of almost 3 times in the surface area of the composite (31 $m^2\ g^{-1}$), revealing the key role of HAP in the improvement of surface properties of the biochar-based composites.

The results evidence that the method used to prepare the multicomposite do not allowed the dispersion of hydroxyapatite

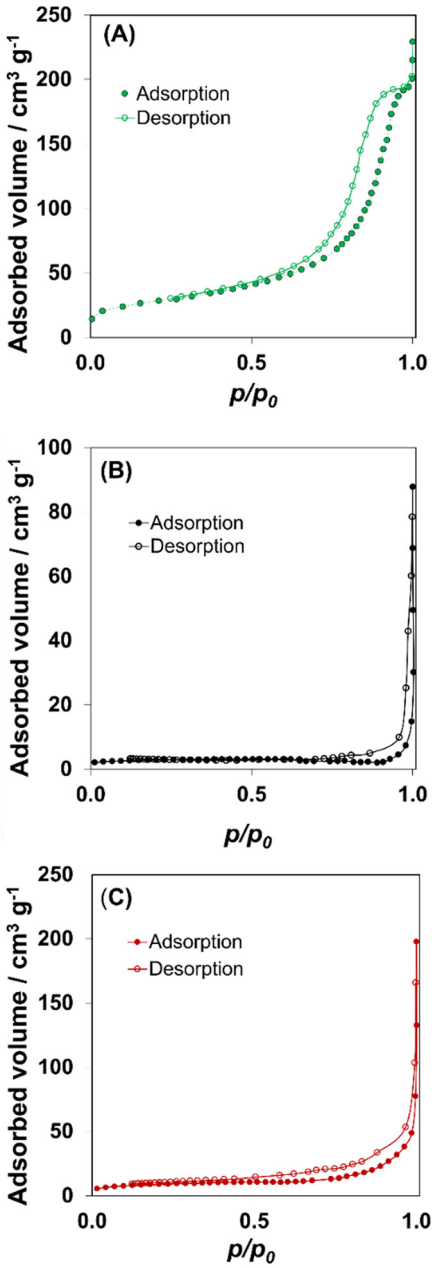

Fig. 2 N_2 adsorption/desorption isotherms collected on (A) HAP; (B) biochar; (C) 10HAP-20Cu/C composite.

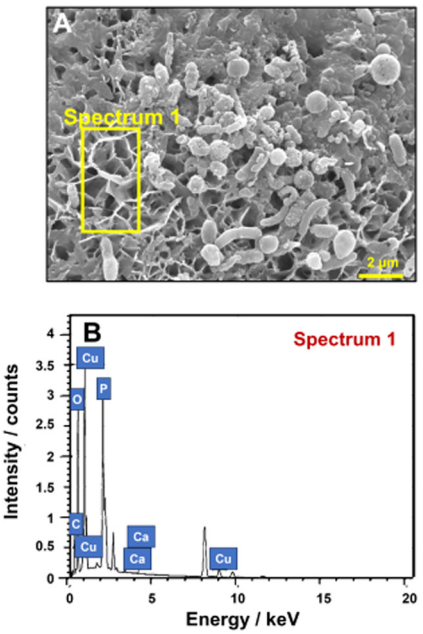

Fig. 3 SEM image of the colonized composite surface (A) and corresponding EDX spectrum of a selected area (B).

nanoparticles inside the multicomposite porosity. Indeed, as already reported in previous work,[46] scanning electron microscopy images revealed that the deposition of HAP occurred exclusively at the external surface area of the biochar (Fig. S1, ESI†). Interestingly, the absence of HAP in the internal section of biochar macropores was also associated with a lack of colonization by microorganisms. The energy dispersive spectra collected on colonized area (Fig. 3) showed typical peaks belonging to P, Ca and Cu elements signifying that a preferential colonization of the surface occurred where HAP was deposited. This evidence points HAP as a possible preferential substrate for the growth of methanogen microorganisms. In fact, the presence of hydrophilic components plays a pivotal role in shaping the interaction dynamics between electroactive microorganisms and their environment, as highlighted in recent studies.[23,58] Hydrophilic moieties not only affect the adherence and distribution of microorganisms but also exert a significant influence on their growth patterns. Consequently, these properties have a direct impact on the electrocatalytic performance of the entire system. The affinity of microorganisms towards hydroxyapatite surface can derive from the peculiar environment which characterized the bio-interface generated by amphoteric hydroxyapatite in water.[59–63]

It is known that mineral-microorganisms interactions are formed *via* electrostatic forces and hydrogen bonds.[64] In the case of HAP such interactions are mediated by numerous acid/basic functionalities present at HAP surface (*e.g.*, PO_4^{3-} and OH^- groups).

Surface acid and basic sites of HAP were then quantified by solid–liquid phase titrations using solutions of 2-phenylethylamine (PEA) and phenyl acetic acid (PAA), selected as basic and acidic probe molecules, respectively. Experimental adsorption isotherms are depicted in Fig. 4. From the I run adsorption of PEA or PAA the total amount of acidic or basic sites could be determined by applying the Langmuir equation to the experimental adsorption data. The II run adsorptions are referred exclusively to weak acidic/basic sites.

Therefore, the difference between the total amount of sites and the amount of the weak sites gives an estimation of the amount of strong acidic or basic sites.

In general, the expected amphoteric nature of HAP was confirmed in terms of amount of total acidic and basic sites with a slight predominance of acid sites (341 *vs.* 261 μeq g^{-1}, respectively). Interestingly, the number of strong sites was the same for basic and acidic sites (*ca.* 188 μeq g^{-1} in both cases),

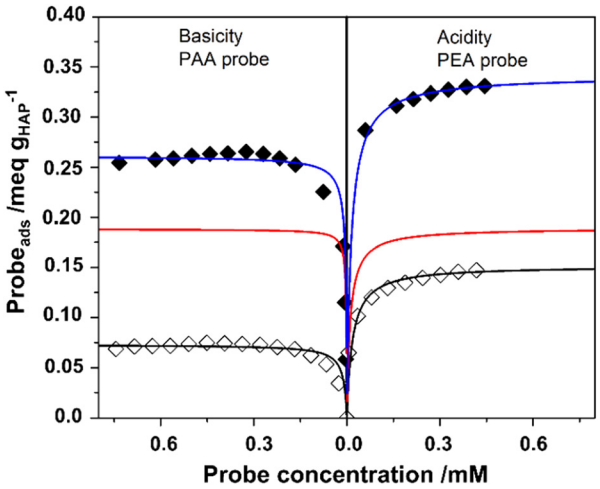

Fig. 4 Adsorption isotherms of PEA (for acidity) and PAA (for basicity) probes at 30 °C on HAP samples evaluated in cyclohexane. Full markers and empty markers represent the I° and the II° run adsorptions, respectively. Red lines represent calculated Langmuir curves of PEA and PAA adsorptions on strong acid and base sites; black lines represent the calculated Langmuir curves of the II° runs; blue lines represent the adsorption trends of the I° runs, obtained as sum of red and black lines.

thus resulting in a ratio between strong acid and basic sites equal to 1, well reflecting the amphoteric character of HAP surface. It should be noted that previous measurements carried out by our group with the same experimental approach, using PEA and benzoic acid as probe molecules, reported a lower total number of sites (159 and 199 μeq g^{-1} for acid and basic sites, respectively) and a slight predominance of basic character for the surfaces of HAP samples precipitated at 80 °C (IA/IB ratio of 0.80).[65]

However, it is known that the interactions between probe molecules and surfaces strongly depend on the nature and charge of surfaces and on the pK_a and chemistry of the probe.[66]

The temperature programmed desorption (TPD) of NH_3 and SO_2 was carried out to on hydroxyapatite (Fig. S2, ESI†). The NH_3-TPD profile revealed that HAP possessed acid sites of medium acid strength, indicated by a desorption band ranging from 350 °C to 400 °C. These acid sites accounted for only 21% of the total desorbed NH_3, with most of the ammonia desorbing at 150 °C, indicative of physisorption or interaction with weak acid sites. Regarding the SO_2 desorption profile, a dominant broad peak was observed, encompassing 78% of the desorbed SO_2 and spanning a wide temperature range from 350 °C to 550 °C. This pronounced peak suggests the presence of basic sites of high strength, which can be attributed to lattice OH^- groups within the apatite structure, as supported by literature.[67]

The amphoteric behaviour of HAP surface derives from the simultaneous presence of Ca^{2+} and PO–H acidic sites (Lewis and Brønsted acid sites, respectively) and OH, PO_4^{3-} and Ca^{2+} vacancies (basic sites). Moreover, even carbonates (incorporated in HAP lattice due to the exposure to air) could play a role in terms of surface acidity-basicity.[68,69] The presence of all these functional groups was corroborated by FT-IR spectroscopic analysis (Fig. S3, ESI†). FT-IR spectrum of HAP samples exhibits the characteristic structural bands of HAP: stretching vibration modes of O–H (3574 cm^{-1}), P–O combination bands of phosphates (565 cm^{-1}, 605 cm^{-1}, 963 cm^{-1} and 1030–1100 cm^{-1}), C–O from carbonates (1500–1350 cm^{-1}).[70]

Besides regulating the interactions with the microorganisms, these functional groups confer interesting chemical reactivity. Actually, when hydroxyapatite encounters water, it forms disordered hydrated layers at the surface and partially dissolves, releasing its constituent ions (calcium cations, phosphates, and hydroxyl ions).[71,72] As a result, the presence of these ions, determines the pH at the electrode/solution interface. In fact, when HAP is contacted with aqueous solutions, these ions impose a pH between 6 and 8 at HAP/solution interface,[73] resulting in a pH buffering action, likely responsible for the remarkable stabilization of pH values observed during electromethanogenesis tests over 200 h, when HAP was included in the composition of biocathode materials (Fig. S4, ESI,† blue line).

It must be underlined that methanogenesis can benefit of pH stabilization by HAP as it is inhibited more than other bioelectrochemical processes when the pH on the cathode rises over 8.[74,75] The pH control under 8, furthermore, can inhibit the deactivation of the cathode that occur in time due to carbonate deposition in carbonate buffered solutions.[76]

The highly hydroxylated surface of HAP could also effectively interact with reagents and products of CO_2 reduction processes. Several studies have reported that the presence of groups able to provide hydrogen-bonding interactions is beneficial for electroreduction processes, since it facilitates easy proton transfer and stabilize key intermediates.[77–82]

HAP is known to strongly adsorb CO_2 molecules through interactions with surface OH^- and O^{2-} basic sites.[83]

However, although CO_2 is usually supplied in the cathodic chamber of BES by directly fluxing gaseous CO_2 at a controlled flow, $CO_{2(g)}$ cannot be the direct carbon source in the reduction reaction at cathode surface, since it dissolves forming $CO_{2(aq)}$ and establishing an equilibrium with bicarbonate anions $HCO_3^-{}_{(aq)}$. Even if bicarbonate represents the predominant form of CO_2 in aqueous solutions, its direct reduction is known to be difficult as well, due to the repulsion between this anionic species and the negatively charged surface of cathode. For this reason, dissolved $CO_{2(aq)}$ adsorbed at the cathode is expected to be the main reagent species. Nevertheless, *in situ* spectroscopic, isotopic labeling, and mass spectrometric experiments have demonstrated that bicarbonate has a beneficial role in the electroreduction of CO_2 since it enhances the reaction rate by increasing the effective reducible concentration of $CO_{2(aq)}$ near the electrode surface.[84,85]

The bicarbonate uptake by biochar, HAP and 10HAP-20Cu/C composite was then evaluated by retro-titrations. While biochar was not able to retain bicarbonate anions, the hydroxyapatite surface, embedding numerous acid and basic functionalities, resulted to be an effective adsorbent for bicarbonate anions (92.5 μmol g^{-1} at 30 °C, Fig. 5). The insertion of carbonates in the HAP lattice took place at the expense of phosphates (B-type substitution). Indeed, FT-IR spectrum after adsorption experiment presents B-type carbonation, as identified by the increase

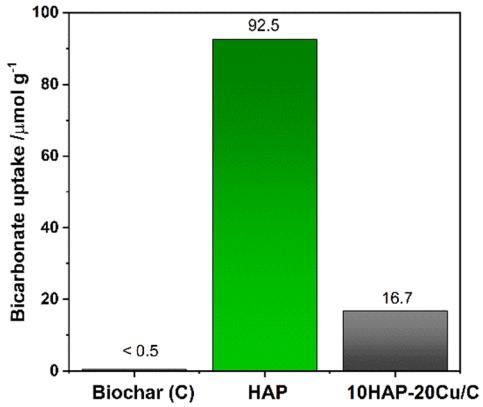

Fig. 5 Bicarbonate uptake by biochar, HAP, 10HAP-20Cu/HAP at 30 °C determined by retro-titrations.

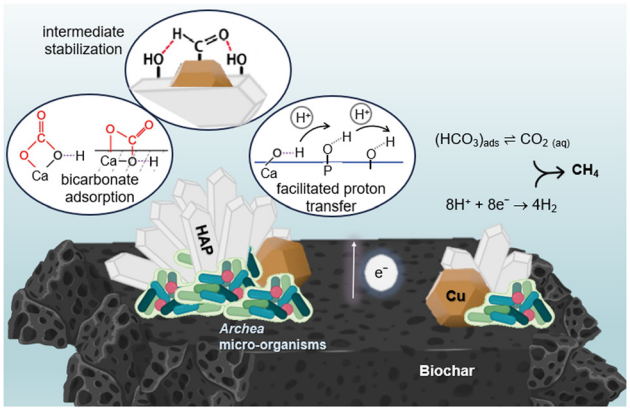

Scheme 1 Potential implications of the HAP Interface in electromethanogenesis processes: beside fostering the adhesion and proliferation of microorganisms, the amphoteric and highly hydrophilic nature of HAP surfaces enhances the availability of reagent species (such as $CO_{2(aq)}$ and $H_{(aq)}^{+}$) at the electrode interface. This is achieved through the adsorption of carbonate species, which are in equilibrium with $CO_{2(aq)}$, and by facilitating proton transfer. Furthermore, HAP potential lies in stabilizing intermediates, promoting their rapid combination with H^+ over desorption, thus facilitating the progression of reduction reactions towards methane formation.

in the intensity of bands at 1419 and 1456 cm^{-1} and 1545 and 1456 cm^{-1} (Fig. 6).

The adsorption capacity of HAP was incorporated by the composite, which was able to retain up to 17 μmol g^{-1} of bicarbonate anions at 30 °C (Fig. 5). The enhanced bicarbonate adsorption associated with HAP presence in the composite could then explain the improved performance in CO_2 reduction. Actually, the interphase enrichment with bicarbonate anions would result in a higher concentration of $CO_{2(aq)}$ at the electrode surface, through rapid equilibrium exchange between these two species (Scheme 1).

To evaluate possible adsorption mechanisms on the substrate surface (*i.e.* hydrogen) and an evolution of the attachment of microorganisms, the electrochemically active surface (ECSA) of the material was obtained by *in situ* monitoring the C_{dl} each week from day 1 to day 14. Cyclic voltammograms at 50 mV s^{-1} of both unpolarized (OCP) and polarized (POL) samples are displayed in Fig. 7.

Graphs of each sample appear with a typical capacitive shape that gives information on the actual active area of the electrode. The unpolarized sample shows a higher capacitive behavior, exposing a higher electrochemically active surface area to the solution. On the other hand, the polarized sample (POL) appears more resistive, possibly due to the adsorption of chemical species on the surface.

We may suggest, based on the poised potential of −1.2 V *vs.* Ag/AgCl, that the molecular hydrogen thermodynamically produced on the surface of the electrode according to eqn (2) is more likely adsorbed and accumulated on the surface close to HAP making it more resistive.

This hypothesis points to an indirect mechanism of methane formation from CO_2 and adsorbed hydrogen by the methanogen organisms settled on the HAP.

Table 1 resumes the ECSA computation based on the C_{dl} obtained, considering that the analysis does not involve any Faradaic reaction. This calculation was carried out using a

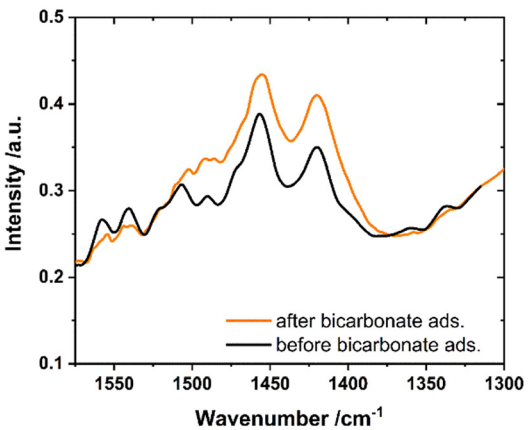

Fig. 6 Magnification of 1300–1600 cm^{-1} region of the FT-IR spectra of HAP before and after bicarbonate adsorption.

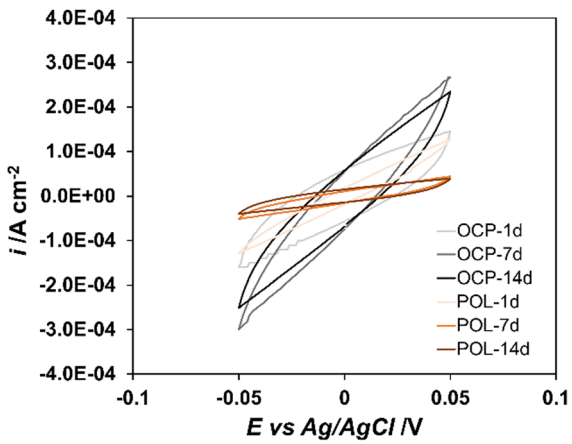

Fig. 7 Cyclic voltammograms at 50 mV s^{-1} of the composite under stationary conditions (OCP) and polarization (−1.2 *vs.* Ag/AgCl) at 1, 7 and 14 days of immersion.

Table 1 Double layer capacitance, C_{dl}, and electrochemically active surface area, ECSA, values obtained on OCP and POL samples after 1, 7 and 14 days of operation. The specific capacitance, C_s, was considered equal to 7.5 μF cm^{-2}

20Cu10HAP	Day	C_{dl}/μF cm^{-2}	ECSA/cm^2
Unpolarized (OCP)	1	$6.4 \times 10^{-1} \pm 7.3 \times 10^{-3}$	$8.6 \times 10^{-2} \pm 9.7 \times 10^{-4}$
	7	$6.4 \times 10^{-1} \pm 7.0 \times 10^{-2}$	$8.5 \times 10^{-2} \pm 9.4 \times 10^{-3}$
	14	$8.4 \times 10^{-1} \pm 1.0 \times 10^{-1}$	$1.1 \times 10^{-1} \pm 1.4 \times 10^{-2}$
Polarized (POL)	1	$1.2 \times 10^{-1} \pm 4.1 \times 10^{-3}$	$1.5 \times 10^{-2} \pm 5.4 \times 10^{-4}$
	7	$1.8 \times 10^{-1} \pm 1.2 \times 10^{-3}$	$2.4 \times 10^{-2} \pm 1.6 \times 10^{-4}$
	14	$2.4 \times 10^{-1} \pm 2.1 \times 10^{-2}$	$3.2 \times 10^{-2} \pm 2.8 \times 10^{-3}$

reference value of 7.5 μF cm^{-2} according to previous studies.[46] As can be seen, the C_{dl} and consequently the ECSA differ according to the poised polarization. Particularly, in the unpolarized sample (OCP), the electron transfer seems to be facilitated according to the ECSA values of 0.08 to 0.1 cm^2. It hence results 8 times higher than the polarized sample (from 0.01 to 0.03 cm^2), confirming the adsorption of chemical species at the interface. A slight increase of the ECSA is also evidenced for both samples at 14 days of operation, possibly suggesting that a more homogeneous layer of biofilm could cover the electrode, contrasting the hydrogen accumulation.

To further assess the nature of chemicals on the composite surface, cyclic voltammograms were recorded in a wider range (−1.5 V *vs.* OCP to 1.5 *vs.* OCP) for both the polarized (orange line) and unpolarized sample (black line). Fig. S5 (ESI†) shows two different shapes of the voltammograms. No reduction/oxidation peaks were observed for the unpolarized sample possibly suggesting a null interaction between the electrode with the solution or the bacteria in the production of chemical species. On the other hand, the voltammogram of the polarized sample shows many different reduction and oxidation peaks, which could hint to hydrogen evolution reaction (either microorganism mediated or not) to produce different chemicals as volatile fatty acids, already detected in a previous work.[12] Interestingly, the large cathodic peak between −500mV and −700 mV (inset) is consistent with hydrogen reduction at pH 7, suggesting a partial adsorption of the electrochemically produced hydrogen on the composite surface. Anyway, a comprehensive understanding of the role of hydroxyapatite and its implications in the electromethanogenesis mechanism will require the use of *in situ* and/or *operando* characterization techniques,[86] able to provide access to in-depth information on electron transfer pathways and catalytic reaction products and intermediates.

Conclusions

Based on these results and assumptions, it can be summarized that hydroxyapatite in biocathode composite materials increases the active interface promoting CO_2 conversion to CH_4 in electromethanogenesis systems. The surface area of hydroxyapatite-containing composite is approximately 3 times higher than that of undoped biochar. Moreover, the exposure of acidic and basic sites at the HAP/solution interfaces would have multiple benefits: *i.e.*, (i) facilitating the adhesion and growth of microorganisms; (ii) acting as a pH buffer; (iii) promoting the adsorption of reacting species (protons, bicarbonate anions), increasing their local concentration at the electrode/solution interface and beneath methanogen microorganisms, (iv) providing stabilization of reaction intermediates by hydrogen bonding with positive implications in terms of a faster reaction kinetics. Based on these observations, we envision that the study of the active HAP-based interface for promoting CO_2 bioelectroreduction will help in the design of composite biomaterials with enhanced performances. Further studies are still needed to identify the reaction mechanism and to corroborate our hypotheses by probing the interface through *in situ* FT-IR spectroscopy.

Author contributions

The contributions of the authors to this work is as follows: Conceptualization, S. C.; methodology, S. C., A. G.; formal analysis, S. C.; laboratory work, M. B., G. G; writing – original draft preparation, M. B., G. G., S. C.; writing – review and editing, S. C., P. C.; supervision: S. C.; project administration: A. G.; funding acquisition: P. C. All authors have read and agreed to the published version of the manuscript.

Conflicts of interest

There are no conflicts to declare.

Acknowledgements

This work has been financed by the Research Fund for the Italian Electrical System under the Contract Agreement between RSE S.p.A. and the Ministry of Economic Development – General Directorate for the Electricity Market, Renewable Energy and Energy Efficiency, Nuclear Energy in compliance with the Decree of April 16th, 2018. Dr Sebastiano Campisi and Prof. Antonella Gervasini acknowledge the REACT EU resources by the NOP Research and Innovation 2014–2020. The technical and scientific staff of Università degli Studi di Milano (Laboratorio di Analisi of Dipartimento di Chimica), in particular Dr Stefania Vitali and Mrs Manuela Gilberti are acknowledged for performing XRD and XPS analyses. Mr Ulisse Della Vittoria and Mr Luca Previtali are gratefully acknowledged for their experimental support.

Notes and references

1 P. Roy, A. K. Mohanty and M. Misra, *Environ. Sci.: Adv.*, 2023, **2**, 409–423.
2 IRENA, *Renewable Energy Statistic*, 2021, **56**.
3 N. Aryal, Y. Zhang, S. Bajracharya, D. Pant and X. Chen, *Chemosphere*, 2022, **291**, 132843.
4 N. N. Horváth-Gönczi, Z. Bagi, M. Szuhaj, G. Rákhely and K. L. Kovács, *Fermentation*, 2023, **9**, 610.
5 Z. Zhang, Y. Song, S. Zheng, G. Zhen, X. Lu, K. Takuro, K. Xu and P. Bakonyi, *Bioresour. Technol.*, 2019, **279**, 339–349.
6 T. Kumar and S. E. Jujjavarappu, *Total Environ. Res. Themes*, 2023, **5**, 100023.
7 L. Liu and D. Pant, *Sustainable Energy Fuels*, 2024, **8**, 460–480.
8 H. Chen, O. Simoska, K. Lim, M. Grattieri, M. Yuan, F. Dong, Y. S. Lee, K. Beaver, S. Weliwatte, E. M. Gaffney and S. D. Minteer, *Chem. Rev.*, 2020, **120**, 12903–12993.
9 R. Conrad, *Pedosphere*, 2020, **30**, 25–39.
10 N. S. Spinner, J. A. Vega and W. E. Mustain, *Catal. Sci. Technol.*, 2012, **2**, 19–28.
11 K. Rabaey and R. A. Rozendal, *Nat. Rev. Microbiol.*, 2010, **8**, 706–716.
12 Y. Tian, J. Wu, D. Liang, J. Li, G. Liu, N. Lin, D. Li and Y. Feng, *Environ. Sci. Technol.*, 2023, **57**, 6733–6742.
13 B. S. Zakaria and B. R. Dhar, *Bioresour. Technol.*, 2019, **289**, 121738.
14 S. Zhang, J. Jiang, H. Wang, F. Li, T. Hua and W. Wang, *J. CO_2* Util., 2021, **51**, 101640.
15 L. Cristiani, L. Leobello, M. Zeppilli and M. Villano, *Renewable Energy*, 2023, **210**, 355–363.
16 R. Blasco-Gómez, P. Batlle-Vilanova, M. Villano, M. D. Balaguer, J. Colprim and S. Puig, *Int. J. Mol. Sci.*, 2017, **18**, 1–32.
17 H. Kobayashi, N. Saito, Q. Fu, H. Kawaguchi, J. Vilcaez, T. Wakayama, H. Maeda and K. Sato, *J. Biosci. Bioeng.*, 2013, **116**, 114–117.
18 K. Sasaki, D. Sasaki, M. Morita, S. I. Hirano, N. Matsumoto, N. Ohmura and Y. Igarashi, *Bioresour. Technol.*, 2010, **101**, 3415–3422.
19 Z. Chen, X. Wang and L. Liu, *Chem. Rec.*, 2019, **19**, 1272–1282.
20 Y. Jiang, M. Su, Y. Zhang, G. Zhan, Y. Tao and D. Li, *Int. J. Hydrogen Energy*, 2013, **38**, 3497–3502.
21 M. Villano, F. Aulenta, C. Ciucci, T. Ferri, A. Giuliano and M. Majone, *Bioresour. Technol.*, 2010, **101**, 3085–3090.
22 J. M. Fontmorin, P. Izadi, D. Li, S. S. Lim, S. Farooq, S. S. Bilal, S. Cheng and E. H. Yu, *Electrochim. Acta*, 2021, **372**, 137853.
23 A. Gomez Vidales, S. Omanovic, H. Li, S. Hrapovic and B. Tartakovsky, *Bioelectrochemistry*, 2022, **148**, 108246.
24 D. Carrillo-Peña, R. Mateos, A. Morán and A. Escapa, *Fuel*, 2022, **321**, 123957.
25 L. Wang, Z. He, Z. Guo, T. Sangeetha, C. Yang, L. Gao, A. Wang and W. Liu, *J. Power Sources*, 2019, **444**, 227306.
26 F. Zhou, J. Zhang, Y. Zhang, Y. Wu, Y. Wang and W. Luo, *Coord. Chem. Rev.*, 2024, **509**, 215802.
27 K. Tahir, W. Miran, J. Jang, A. Shahzad, M. Moztahida, B. Kim and D. S. Lee, *Chem. Eng. J.*, 2020, **381**, 122687.
28 M. Siegert, M. D. Yates, D. F. Call, X. Zhu, A. Spormann and B. E. Logan, *ACS Sustainable Chem. Eng.*, 2014, **2**, 910–917.
29 N. Liu, K. Tang, D. Wang, F. Fei, H. Cui, F. Li, J. Lei, D. Crawshaw, X. Zhang and L. Tang, *Sep. Purif. Technol.*, 2024, **332**, 125873.
30 N. Liu, B. Hu, K. Tang, T. Xia, F. Li, G. Quan, X. Zhang and L. Tang, *Surf. Interfaces*, 2023, **41**, 103134.
31 N. Liu, M. Tang, J. Wu, L. Tang, W. Huang, Q. Li, J. Lei, X. Zhang and L. Wang, *Adv. Mater. Interfaces*, 2020, **7**, 1–11.
32 K. Wang, D. Huang, L. Yu, K. Feng, L. Li, T. Harada, S. Ikeda and F. Jiang, *ACS Catal.*, 2019, **9**, 3090–3097.
33 R. Li, T. Gao, Y. Wang, Y. Chen, W. Luo, Y. Wu, Y. Xie, Y. Wang and Y. Zhang, *Int. J. Hydrogen Energy*, 2024, **63**, 1116–1127.
34 F. Kracke, A. B. Wong, K. Maegaard, J. S. Deutzmann, M. K. A. Hubert, C. Hahn, T. F. Jaramillo and A. M. Spormann, *Commun. Chem.*, 2019, **2**, 1–9.
35 A. Gomez Vidales, G. Bruant, S. Omanovic and B. Tartakovsky, *Electrochim. Acta*, 2021, **383**, 138349.
36 Z. Qiu, K. Zhang, X. L. Li, T. S. Song and J. Xie, *Biochem. Eng. J.*, 2023, **192**, 108842.
37 M. T. Vu, D. Thatikayala and B. Min, *Int. J. Hydrogen Energy*, 2022, **47**, 1121–1131.
38 M. T. Vu, M. T. Noori and B. Min, *Chem. Eng. J.*, 2020, **393**, 124613.
39 M. Ferri, S. Campisi, L. Polito, J. Shen and A. Gervasini, *J. Hazard. Mater.*, 2021, **420**, 126656.
40 M. Magni, D. Sironi, M. Ferri, S. Trasatti, S. Campisi, A. Gervasini, M. Papacchini and P. Cristiani, *ChemElectroChem*, 2023, **10**, 1–10.
41 M. Ibrahim, M. Labaki, J.-M. Giraudon and J.-F. Lamonier, *J. Hazard. Mater.*, 2020, **383**, 121139.
42 S. Campisi, M. Leone, M. Papacchini, C. Evangelisti, L. Polito, G. Postole and A. Gervasini, *J. Colloid Interface Sci.*, 2023, **630**, 473–486.
43 M. Ferri, L. Delafontaine, S. Guo, T. Asset, P. Cristiani, S. Campisi, A. Gervasini and P. Atanassov, *ACS Energy Lett.*, 2022, **8**, 2304–2310.
44 A. Prado, R. Berenguer and A. Esteve-Núñez, *Carbon*, 2019, **146**, 597–609.
45 P. Cristiani, A. Goglio, S. Marzorati, S. Fest-Santini and A. Schievano, *Front. Energy Res.*, 2020, **8**, 1–12.
46 G. Ghiara, S. Campisi, A. Goglio, F. Formicola, M. Balordi, A. Gervasini, S. P. M. Trasatti, F. Adani, A. Franzetti and P. Cristiani, *Sustainable Energy Technol. Assess.*, 2023, **57**, 103274.
47 A. Fihri, C. Len, R. S. Varma and A. Solhy, *Coord. Chem. Rev.*, 2017, **347**, 48–76.
48 S. Campisi, M. G. Galloni, F. Bossola and A. Gervasini, *Catal. Commun.*, 2019, **123**, 79–85.
49 M. G. Galloni, S. Campisi, A. Gervasini, S. Morandi and M. Manzoli, *Appl. Catal., A*, 2023, **655**, 119101.
50 J. Guo, P. N. Duchesne, L. Wang, R. Song, M. Xia, U. Ulmer, W. Sun, Y. Dong, J. Y. Y. Loh, N. P. Kherani, J. Du, B. Zhu,

W. Huang, S. Zhang and G. A. Ozin, *ACS Catal.*, 2020, **10**, 13668–13681.
51 Y. Peng, H. Szalad, P. Nikacevic, G. Gorni, S. Goberna, L. Simonelli, J. Albero, N. López and H. García, *Appl. Catal., B*, 2023, **333**, 122790.
52 S. Campisi, C. Castellano and A. Gervasini, *New J. Chem.*, 2018, **42**, 4520–4530.
53 D. Schieppati, N. A. Patience, S. Campisi and G. S. Patience, *Can. J. Chem. Eng.*, 2021, **99**, 1663–1682.
54 P. Carniti and A. Gervasini, in *Springer Series in Materials Science*, Springer Science and Business Media Deutschland GmbH, 2013, vol. 154, pp. 543–551.
55 W. Luo and S. Zafeiratos, in *Metal-free Functionalized Carbons in Catalysis: Synthesis, Characterization and Applications Editors: Alberto Villa, Nikolaos Dimitratos*, 2018, pp. 138–176.
56 M. C. Biesinger, *Surf. Interface Anal.*, 2017, **49**, 1325–1334.
57 M. D. Donohue and G. L. Aranovich, *Adv. Colloid Interface Sci.*, 1998, **76–77**, 137–152.
58 M. Sharma, Y. Alvarez-Gallego, W. Achouak, D. Pant, P. M. Sarma and X. Dominguez-Benetton, *J. Mater. Chem. A*, 2019, **7**, 24420–24436.
59 W. B. Clark, L. L. Bammann and R. J. Gibbons, *Infect. Immun.*, 1978, **19**, 846–853.
60 M. Katsikogianni, Y. F. Missirlis, L. Harris and J. Douglas, *Eur. Cells Mater.*, 2004, **8**, 37–57.
61 S. C. Venegas, J. M. Palacios, M. C. Apella, P. J. Morando and M. A. Blesa, *J. Dent. Res.*, 2006, **85**, 1124–1128.
62 E. D. Berry and G. R. Siragusa, *Appl. Environ. Microbiol.*, 1997, **63**, 4069–4074.
63 L. Gelati, M. Rabufetti, M. Benaglia, S. Campisi, A. Gervasini, G. Speranza and C. F. Morelli, *ChemPlusChem*, 2024, e202400204.
64 H. Dong, L. Huang, L. Zhao, Q. Zeng, X. Liu, Y. Sheng, L. Shi, G. Wu, H. Jiang, F. Li, L. Zhang, D. Guo, G. Li, W. Hou and H. Chen, *Natl. Sci. Rev.*, 2022, **9**, nwac128.
65 M. Ferri, S. Campisi, M. Scavini, C. Evangelisti, P. Carniti and A. Gervasini, *Appl. Surf. Sci.*, 2019, **475**, 397–409.
66 N. Zaouri, L. Gutierrez, M. F. Benedetti and J.-P. Croue, *Colloids Surf., A*, 2021, **625**, 126858.
67 L. Silvester, J. F. Lamonier, C. Lamonier, M. Capron, R. N. Vannier, A. S. Mamede and F. Dumeignil, *ChemCatChem*, 2017, **9**, 2250–2261.
68 S. Diallo-Garcia, M. Ben Osman, J. M. Krafft, S. Casale, C. Thomas, J. Kubo and G. Costentin, *J. Phys. Chem. C*, 2014, **118**, 12744–12757.
69 D. Kiani and J. Baltrusaitis, *Chem Catal.*, 2021, **1**, 782–801.
70 L. Silvester, J.-F. Lamonier, R.-N. Vannier, C. Lamonier, M. Capron, A.-S. Mamede, F. Pourpoint, A. Gervasini and F. Dumeignil, *J. Mater. Chem. A*, 2014, **2**, 11073–11090.
71 C. Jäger, T. Welzel, W. Meyer-Zaika and M. Epple, *Magn. Reson. Chem.*, 2006, **44**, 573–580.
72 D. Zahn and O. Hochrein, *Phys. Chem. Chem. Phys.*, 2003, **5**, 4004–4007.
73 Y. A. Attia and D. W. Fuerstenau, *Colloids Surf.*, 1988, **34**, 271–285.
74 P. Cristiani, M. L. Carvalho, E. Guerrini, M. Daghio, C. Santoro and B. Li, *Bioelectrochemistry*, 2013, **92**, 6–13.
75 A. A. Mier, H. Olvera-Vargas, M. Mejía-López, A. Longoria, L. Verea, P. J. Sebastian and D. M. Arias, *Chemosphere*, 2021, **283**, 131138.
76 M. Santini, S. Marzorati, S. Fest-Santini, S. Trasatti and P. Cristiani, *J. Power Sources*, 2017, **356**, 400–407.
77 Y. Wang, M. Liu, G. Gao, Y. Yang, R. Yang, H. Ding, Y. Chen, S. Li and Y. Lan, *Angew. Chem.*, 2021, **133**, 22123–22129.
78 J. Yi, R. Xie, Z. Xie, G. Chai, T. Liu, R. Chen, Y. Huang and R. Cao, *Angew. Chem.*, 2020, **132**, 23849–23856.
79 Y. Wang, N. Y. Huang, H. Y. Wang, X. W. Zhang, J. R. Huang, P. Q. Liao, X. M. Chen and J. P. Zhang, *CCS Chem.*, 2023, **5**, 145–151.
80 Q. J. Wu, D. H. Si, Q. Wu, Y. L. Dong, R. Cao and Y. B. Huang, *Angew. Chem., Int. Ed.*, 2023, **62**, e202215687.
81 C. Zhu, C. D'Agostino and S. P. de Visser, *Inorg. Chem.*, 2024, **63**, 4474–4481.
82 T. Shan, J. Li, S. Wu, H. Wu, F. Zhang, G. Liao, H. Xiao, L. Huang and L. Chen, *Chem. Eng. J.*, 2023, **478**, 147509.
83 M. Miyauchi, T. Watanabe, D. Hoshi and T. Ohba, *Dalton Trans.*, 2019, **48**, 17507–17515.
84 W. Deng, T. Yuan, S. Chen, H. Li, C. Hu, H. Dong, B. Wu, T. Wang, J. Li, G. A. Ozin and J. Gong, *Fundam. Res.*, 2021, **1**, 432–438.
85 M. Dunwell, Q. Lu, J. M. Heyes, J. Rosen, J. G. Chen, Y. Yan, F. Jiao and B. Xu, *J. Am. Chem. Soc.*, 2017, **139**, 3774–3783.
86 J. C. P. de Souza, L. J. A. Macedo, A. Hassan, G. C. Sedenho, I. A. Modenez and F. N. Crespilho, *ChemElectroChem*, 2021, **8**, 431–446.